Case Studies in Thermal Engineering 48 (2023) 103176

Contents lists available at ScienceDirect

Case Studies in Thermal Engineering

journal homepage: www.elsevier.com/locate/csite

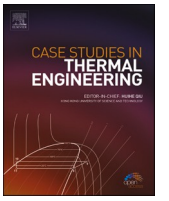

Online monitoring instantaneous 2D temperature distributions in a furnace using acoustic tomography based on frequency division multiplexing

Qi Liu [a], Bin Zhou [a,*], Ruixue Cheng [b], Jianyong Zhang [b], Rong Zhao [a], Minglu Dai [a], Xuhao Zhao [a], Yihong Wang [c]

[a] School of Energy and Environment, Southeast University, Nanjing, 210096, China
[b] School of Computing, Engineering and Digital Technologies, Teesside University, Middlesbrough, TS1 3BA, UK
[c] School of Electronic and Optical Engineering, Nanjing University of Science and Technology, Nanjing, 210096, China

ARTICLE INFO

Keywords:
Temporal resolution
Frequency division multiplexing
Acoustic time of flight
Acoustic tomography
Temperature distribution reconstruction

ABSTRACT

The online and accurate capture of dynamic changes in furnace temperature distribution is crucial for production efficiency improvement and international environmental policy compliance in power plants. To achieve this, a measurement system with a reliable online reconstruction capability and high temporal resolution is necessary. This paper presents a novel technique that can improve the temporal resolution of the currently existing acoustic tomography (AT) system using frequency division multiplexing (FDM). This method allows for concurrent transmissions of acoustic signals in several different frequency bands instead of a sequential manner, which leads to more efficient channel utilization and allows all acoustic signals to be acquired at the same time, so that a better temporal uniformity of multipath acoustic signals can be realized. Theoretical analysis and experiments have been conducted to verify the effectiveness of this technique. The results prove that the proposed method can significantly improve the temporal resolution of the AT system while maintaining the accuracy and robustness of the reconstruction.

1. Introduction

Although renewable energy has gained great attention in recent years, coal-fired power generations still account for a substantial proportion of electricity production at present. Monitoring the temperature distribution inside a boiler is essential for understanding combustion conditions as well as for accurate online monitoring and combustion parameter control to improve efficiency and reduce emissions [1]. The invasive measurement techniques, such as thermocouple thermometers [2], blackbody chamber thermometers [3], and fiber temperature measuring systems [4], have limited practical applications because of severe probe wear due to particles and the slow dynamic response as a result of large cross-section area of furnace. For non-contact measurement techniques, like the tunable diode laser absorption spectroscopy [5–7], infrared thermometry [8], radiation thermometry [9,10], and other methods, they also face problems related to high power consumption on light sources, optical misalignment, readily lens contamination and high equipment costs for temperature tomography imaging. In contrast, acoustic tomography (AT) [11–14] is now widely adopted for monitoring furnace temperature distribution due to its low cost, non-intrusive nature, wide measurement range, and real-time, online monitoring capability.

* Corresponding author.
E-mail address: zhoubinde@seu.edu.cn (B. Zhou).

https://doi.org/10.1016/j.csite.2023.103176
Received 30 November 2022; Received in revised form 3 June 2023; Accepted 8 June 2023
Available online 8 June 2023

Many studies have been devoted to improving the spatial resolution of AT [11,15–17], which has enabled the reconstruction of temperature distribution to be implemented with greater accuracy in real time. However, the insufficient temporal resolution prohibits the current AT system's wider applications because of its incapability of capturing the dynamic changes in temperature distribution due to the fact that it takes 10 s or even longer [18,19] to update a reconstruction of temperature distribution, and such a long delay in practice cannot meet the requirements for instant process diagnosis and control.

The temperature distribution reconstruction of an AT system can be, roughly divided into two stages. The first stage is to arrange multiple loudspeakers (transmitters) and microphones (receivers) around a region of interest (RoI), as shown in Fig. 2. The acoustic signals are received by the microphones after crossing multiple paths of the RoI, and the time of flight (TOF) is estimated by a time delay algorithm [20]. The second stage is to reconstruct the temperature image through specific inversion algorithms using TOFs from multiple paths because the sound speed in the RoI is a function of the temperature of the intervening medium [21]. At stage one of the conventional measurement method, one acoustic wave is transmitted by one loudspeaker at a time and received by the corresponding microphones. The complete measurement cycle is the process in that each of the multiple loudspeakers is switched on and off sequentially to complete measurements for S number of loops (S is usually the number of loudspeakers) [14,22,23]. Such a sequential transmission manner poses a significant problem when the ambient temperature varies during the acquisition period as the signals from multiple paths are not acquired in the same time frame， thus significantly diminishing the AT system's value unless the ambient temperature has been constant.

Extensive research efforts have been invested in an attempt to improve the temporal resolution of AT systems, which can be broadly classified into the following categories: (1) Reducing the operational complexity [24] and the iteration number [19,25] of the inversion algorithm, hence reducing the computation time so that the time for reconstruction in the second stage is reduced. However, the improvement of time resolution by this revised reconstruction algorithm is insignificant since the time consumption is largely at stage one for the acoustic signal transmission and acquisition. (2) Enhancing hardware capabilities, such as upgrading the computer's performance and adding an internal high-speed data acquisition system [18] to elevate the temporal resolution. However, since the logic and time series of signal acquisition are deterministic, the time saved from the single acquisition speed of the hardware can only be minimal. (3) Reducing the number of TOFs per frame [12] or reducing the number of projections [26], thus speeding up the data acquisition. The consequent problem of the rank-deficiency [25] due to the reduction in the number of input conditions can then be compensated using algorithmic optimization methods [19,27], such as nonlinear laminar imaging [28], compressed perception [29–31], adding virtual projection data [32], or through exploiting the redundancy of the temporal information [12,26]. Although this method can also elevate the temporal resolution, the adverse effect will inevitably cause degradation of the reconstruction accuracy and increase the risk of discrete ill-posed problems [33].

Although the above-mentioned studies have improved the temporal resolution of the AT system to some extent, the fundamental issue of capturing unsynchronized signals from multipath still remains. To address this problem, we propose a frequency division multiplexing (FDM)-based AT system that enables acoustic signals from multiple frequency bands to be transmitted simultaneously and share the same physical channel. This approach allows all microphones to receive the signals at the same moment, which not only reduces the time needed for signal transmission and acquisition, resulting in significantly improved temporal resolution but also eliminates the problem of non-uniformity in the signals' timing. As a result, this system can provide real-time and accurate temperature reconstruction.

2. Methodology

2.1. Acoustic tomography

The theoretical basis of the AT system is the mathematical relationship between sound speed and temperature [34] :

$$c=\sqrt{\frac{\gamma R}{M}T}=\frac{L}{\tau},\ \text{or}\ T=\frac{M}{\gamma R}\left(\frac{L}{\tau}\right)^2 \tag{1}$$

where c defines the speed of sound, γ is the adiabatic exponent of the gaseous medium, R is the universal gas constant of the ideal gas, M is the molar mass of the gaseous medium, and T stands for the gas temperature; while L is the distance between the loudspeaker and the

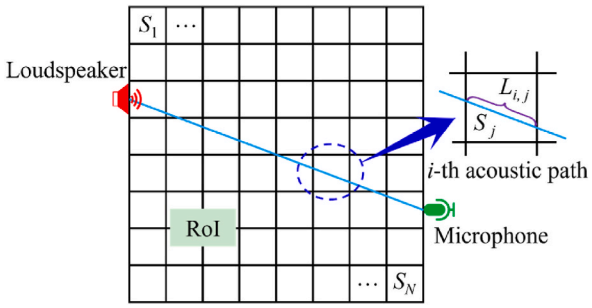

Fig. 1. Geometric description of AT reconstruction in the discretized RoI.

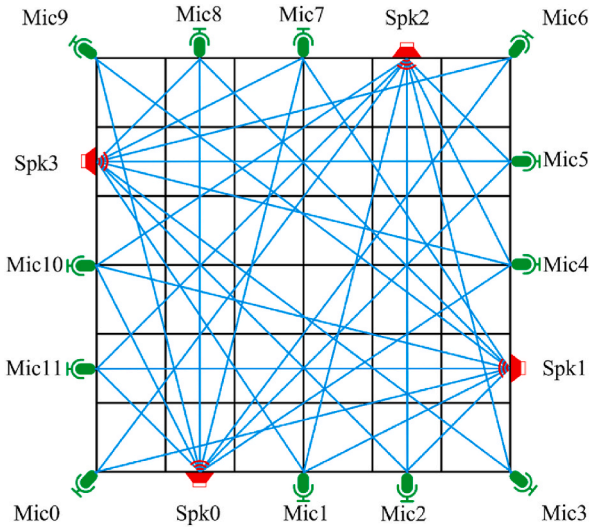

Fig. 2. The acoustic tomography setup with four loudspeakers and twelve microphones.

microphone, and τ is the TOF.

The RoI is quantized into N non-overlapping pixel regions, as shown in Fig. 1, where the gas's temperature, pressure, and molar mass are uniform within each pixel. The sensors are arranged in such a way that the acoustic signals are transmitted and received by loudspeakers and microphones, respectively, to measure the TOF along each acoustic path for temperature distribution measurement. The temperature distribution of RoI affects the sound speed distribution, resulting in an increase or decrease of the TOF. For a typical electric furnace environment, the refraction effect of acoustic propagation inflicts the accuracy degradation of the constructed tomographic image. However, according to Green's analytical study of tomographic measurement errors in localized high-temperature fields, the refraction effect gives rise to about 2% reconstruction error in the worst case [35]. Therefore, straight ray propagation, a hypothetical model of the acoustic signal between the loudspeaker and the microphone was used in this study for simplicity [12, 36–38].

Based on the straight ray model, the TOF is defined as:

$$\tau = \int_L \frac{1}{c_{\text{eff}}} dL = \int_L S(x,y) dL \tag{2}$$

where τ is the TOF measurement, c_{eff} is the effective speed of sound along the path element. The slowness S (x, y) is defined as the reciprocal of the effective speed of sound. c_{eff} is composed of the Laplace speed of sound $c_L(T)$ and the gas flow velocity v in the direction of sound propagation [21],

$$c_{\text{eff}}(T, v) = c_L(T) + v \tag{3}$$

Since no significant gas flow is involved in this study, the small effect of v is negligible, so it can be approximated that the gas flow rate v is much smaller than $c_L(T)$. As shown in Fig. 1, the TOF of the i-th acoustic path for the RoI is given by

$$\tau_i = \sum_{j=1}^{N} L_{i,j} S_j \tag{4}$$

where $L_{i,j}$ represents the length of the i-th acoustic path within the j-th pixel, $S_j = 1/c_{L,\,j}(T)$ is defined as the slowness in the j-th pixel.

For an AT system with M acoustic paths, Eq. (4) can be formulated as a linear equation

$$LS = \tau + r_{\text{noise}} \tag{5}$$

where $L \in \mathbb{R}^{M \times N}$ is the path matrix, $S \in \mathbb{R}^N$ is the vector of pixel-wised slowness S_j (j = 1,2, …,N) to be solved in the inverse problem, $\tau \in \mathbb{R}^M$ is the measured TOF, and r_{noise} is the system noise.

In field applications, the arrangement of loudspeakers and microphones is constrained by practicality, and it is impossible to arrange numerous acoustic paths. Therefore, the actual measurement conditions are generally $M < N$, making the L a large sparse matrix, which then leads to an ill-posed problem for the inversion that can consequently lead to no valid solution.

In this study, the simultaneous algebraic reconstruction method (SART) [19,27], a compromise between the ART and SIRT methods, is used to overcome the ill-posed problem and improve the reconstruction efficiency of the AT system. The robustness of SART is better than the ART method, and the number of iterations for convergence is less than that of the SIRT method [19].

The iteration scheme can be written as follows:

$$S_j^{k+1} = S_j^k + \frac{\lambda}{\sum_{i=1}^{M} L_{ij}} \cdot \sum_{i=1}^{M} \frac{\tau_i - \sum_{j=1}^{N} L_{ij} S_j^k}{\sum_{j=1}^{N} L_{ij}} L_{ij} \tag{6}$$

where the superscript k indicates the iteration number, $\lambda \in (0,2)$ is the relaxation factor that dictates the convergence rate of the iterative process [39].

2.2. TOF measurement method with a high temporal resolution

In the sensor arrangements shown in Fig. 2, the Spk and Mic denote loudspeaker and microphone, respectively. In a conventional AT system, each of the loudspeakers is switched on and off sequentially transmitting identical acoustic signals to their corresponding microphones [14,19,23,40]. That is, the sound source signal is transmitted by Spk0 and received by Mic4-Mic11 at the same time, then the same sound source signal is transmitted by Spk1 and received by Mic7-Mic11 and Mic0-Mic2 simultaneously, and this is repeated by the Spk2 and Spk3 and their microphones as depicted in Fig. 2 and in a time sequence outlined in Fig. 3(a). It is important to note that the interval between two loudspeaker transmissions is set longer than the reverberation time T_{60} [34,41]. This is to avoid the echo and reverberation inflicted by multiple reflections of acoustic waves in a confined space, thus its interference with the TOF measurements can be minimized. The TOF measurement period of the conventional method of tomography is given by,

$$t_{\text{conventional}} = 4(\tau_s + \tau + \triangle\tau) \tag{7}$$

where τ_s is the pulse width of the acoustic source signal, τ is assumed to be the TOF of the acoustic wave received by the microphone at the longest distance, and $\Delta\tau$ is set as the time interval switching between the loudspeakers.

The proposed FDM measurement method in this paper is that the signal to be transmitted is divided into four acoustic waves that do not overlap in the frequency domain, and a certain number of frequency bands are spaced between the channels to avoid interference from adjacent bandwidths. Signals with different bandwidths are transmitted concurrently by all the loudspeakers, thus creating parallel measurements in time without causing spectral interference. Apparently, such an approach requires only one transmission and receiving time, instead of repeating the process in turn for all 4 Spks, giving a substantial time reduction, hence a significant improvement in temporal resolution can be achieved. As shown in Fig. 3(b), the TOF measurement period for the FDM method of tomography is

$$t_{\text{FDM}} = \tau_s + \tau + \triangle\tau \tag{8}$$

For the sensor arrangement depicted in Fig. 2, a comparison of (7) and (8) can show that the TOF measurement time of the FDM method is only 0.25s or a quarter of that of the conventional method. Thus the FDM method offers not only a higher temporal resolution but also enables to achieve of the concurrence of signals along all the acoustic paths.

2.3. Acoustic source signal

The signal model with linear variation in frequency [42,43] has been proven to differentiate signals more effectively from noise, leading to improved Signal to Noise Ratio (SNR) [44,45]. This research modulates the acoustic source signal using Chirp's widely used linear frequency. Assuming the presence of additive noise of both the loudspeaker and microphone, the transmitted signal $x_1(t)$ and received signal $x_2(t)$ are expressed as:

$$\begin{cases} x_1(t) = s(t) + \mu_1(t) \\ x_2(t) = \xi s(t-\tau) + \mu_2(t) \end{cases} \tag{9}$$

where $s(t)$ is the acoustic source signal. $\mu_1(t)$ and $\mu_2(t)$ are the random noises contained in the signals. ξ is the attenuation coefficient of the acoustic signal. τ denotes the TOF between the transmitted and received signals. $s(t)$, $\mu_1(t)$, and $\mu_2(t)$ are assumed to be uncorrelated.

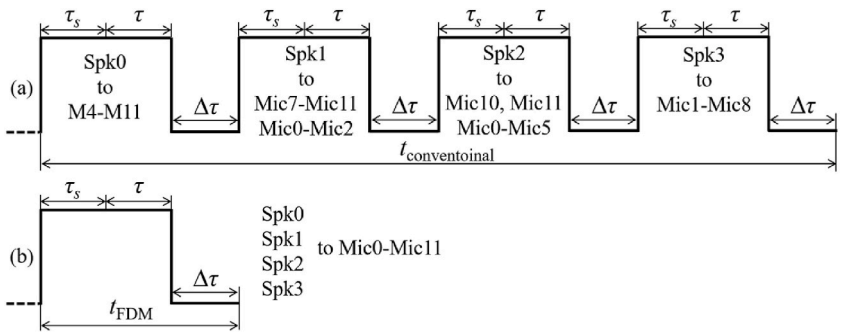

Fig. 3. (a) and (b) are the timing diagrams of TOF measured by conventional and FDM methods.

The transmitted signal $x_1(t)$ is

$$x_1(t) = A\cos\left(2\pi f_{\text{Chirp}} t + \Delta\varphi\right) + \mu_1(t)\ t \in [0, \tau_s] \tag{10}$$

where A is the signal amplitude, φ is the signal phase. f_{Chirp} denotes the sweeping frequency of the signal, which is expressed as:

$$f_{\text{Chirp}} = f_0 + \frac{B_w}{\tau_s} t\ t \in [0, \tau_s] \tag{11}$$

where f_0 is the initial starting frequency at $t = 0$, B_w is the bandwidth in hertz. The frequency variations of the sources involved in this study are all unidirectional upward frequency-sweeping.

Nonlinear problems are complex and varied, and the typical type of nonlinear distortion in electroacoustic systems is harmonic distortion [46]. The signal $X(t)$ received by a nonlinear system can be approximated in polynomial form as:

$$X(t) = a_1 x(t) + a_2 x^2(t) + a_3 x^3(t) + \ldots + a_n x^n(t) \tag{12}$$

where $x(t)$ denotes the Chirp signal in (9) and a_n is the coefficient of the nth nonlinear order. In nonlinear acoustics, it is generally assumed that it decreases exponentially with the order, and the nonlinear distortion gradually decreases with the order increase. In this study, the most influential second harmonic is considered. Appropriate selection of the frequency band of the sound source signal is key to avoiding interference, as four loudspeakers are transmitting concurrently.

Fig. 4(a) shows the time-frequency relationship for the four source models. The pulse widths of the four Chirp sources are 0.2s, and the starting frequencies are 1.5 kHz, 5.5 kHz, 7.5 kHz, and 9.5 kHz, respectively, with a bandwidth of 1 kHz. There is no source signal in the frequency range of 3 kHz–5kHz adopted to avoid the influence of the second harmonic of the 1.5kHz–2.5 kHz signal of Spk0. The second harmonic range of the source signals of Spk1- Spk3 is all greater than 11 kHz, so none of the four sources set are affected by the second harmonic. In addition, the interval between the termination frequency of the sound source and the starting frequency of the next one, starting from Spk0, is all greater than 1 kHz, facilitating that the signals received by the microphone can be accurately separated by the method described in Section 2.5.

2.4. Cramer-Rao bound analysis for TOF estimation

Based on the fact that the signal frequency band used in this article is within the range of 20 Hz to 20 kHz and the reconstruction accuracy of the temperature field is directly determined by the acoustic TOF, the lower limit of accuracy of the acoustic TOF is estimated in the following analysis. The FDM method proposed in the article divides the original wideband signal into multiple narrowband signals. The estimated accuracy of the TOF of these signals may vary when they pass through the ROI path. Additionally, the source starting frequency and bandwidth of the conventional and FDM methods are different, and thus the estimated accuracy of the TOF for signals with different bandwidths needs to be discussed. In principle, higher the bandwidth is, a more accurate delay estimation can be achieved. Therefore, before using the FDM method to reconstruct the temperature field, it is necessary to measure the error level of the TOF estimation introduced by the signal bandwidth segmentation.

In order to measure the transmission time of sound waves with different bandwidths and determine their lower error limits, the Cramer-Rao lower bound (CRLB) [47,48] is used to calculate the minimum lower error limit. The CRLB refers to the minimum error of measuring a signal, which is a theoretical limit. This ensures the reliability of the measurement results and also provides insights into the limitations and advantages of measuring acoustic TOF for signals with different bandwidths. Due to the limitation of the length of the article and the lengthy derivation process, here is only the mathematical formula for the Cramer-Rao lower bound for TOF estimation:

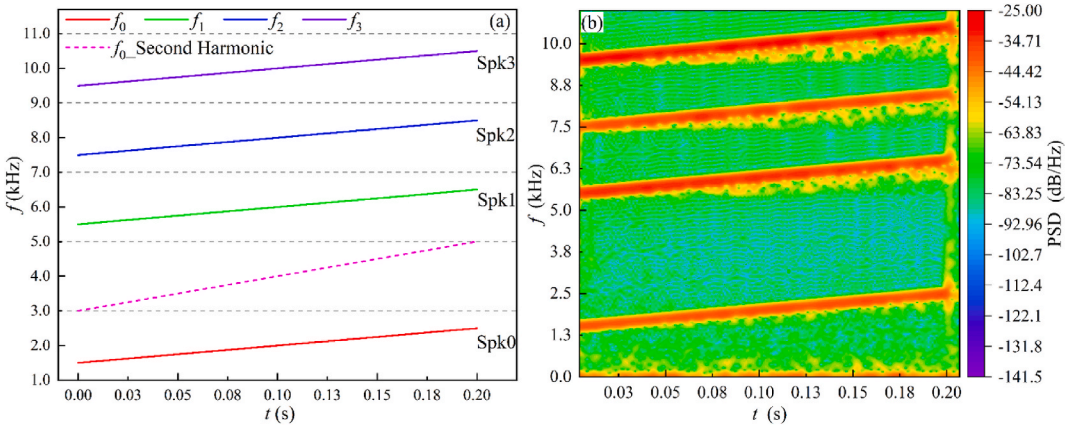

Fig. 4. Time-frequency relationship of acoustic signals. (a) Time-frequency relationship of each loudspeaker's sound source signal. (b) The acoustic spectrum of the signal sampled by M1 when S0–S4 are transmitted simultaneously.

$$Var(\hat{\tau}) \geq \frac{1}{4\pi^2\left(f_0 + \frac{2B_w}{\tau_s}\tau\right)^2 SNR} \tag{13}$$

where $\hat{\tau}$ represents the unbiased estimator of the time-of-flight τ, $Var(\hat{\tau})$ represents the variance of this estimator.

The CRLBs of the TOF estimation for the conventional method ($f_0 = 4$ kHz, $B_w = 2$ kHz) and the FDM method ($f_0 = 1.5$ kHz, 5.5 kHz, 7.5 kHz, and 9.5 kHz, $B_w = 1$ kHz) were calculated based on the derived expressions. The CRLB values of TOF estimation for signals with different starting frequencies and bandwidths were calculated at 21 different SNR levels ranging from −10 dB to 10 dB, as shown in Fig. 5. It can be observed from Fig. 5 that for signals with the same bandwidth, the higher the starting frequency is, the lower the CRLB of the TOF estimation becomes. However, this trend is not fixed but depends on the SNR. As shown in the above figure, with the SNR increases, the correlation between the CRLB and the starting frequency gets weaker.

The CRLB values of the four signals generated by the FDM method are very close to each other, and at the worst SNR level, the difference is only 1.876e-8 s^2. With this level of TOF estimation accuracy, the temperature calculation error for a 1 m distance is only 0.0078 °C, which is negligible compared to the actual temperature range studied in this paper. In addition, it can be seen from Fig. 5 that the CRLB value of the sound source signal in the conventional method is relatively lower than that of the FDM method due to its larger bandwidth (SNR > −1 dB). When SNR = −10 dB, the difference in CRLB values is the largest, but it is only 3.3492e-08 s^2. With this level of TOF estimation error, the temperature deviation is only 0.0068 °C. Therefore, compared with the small error introduced by the segmented signal bandwidth in the FDM method, its high time resolution character is more meaningful. Hence, the TOF estimation error introduced by the difference in signal source bandwidth and starting frequency between the two methods is ignored in this paper.

2.5. Signal analysis and processing by the FDM method

The acoustic signals transmitted simultaneously by the four loudspeakers are superimposed and received by all the microphones, which can then be extracted accurately for TOF estimation, according to the sensor correspondence shown in Fig. 2.

The sampling rate and duration of the system were set to 100 kS/s and 0.21 s, respectively. Each of the four sound signals was amplified with a gain of 10 times. The same set of parameters was set to the device in the experiments which are to be introduced in section 4. Fig. 4(b) presents the acoustic spectrum of the signal received by Mic1. In the sampling duration, there are four distinct linear sweep bands with the same sweep range as shown in Fig. 4(a), indicating that the system can sample multiple source signals simultaneously. Some acoustic spectrum artifacts below 1 kHz and near each band are caused by background noise and intermodulation distortion of the loudspeakers at the acquisition time. Since the cross-correlation algorithm used in estimating the TOF can tolerate local distortion, a lower proportion of distortion is permitted and does not affect the accuracy of the TOF estimation [23]. The interference of background noise can be eliminated in the filtering operation during the signal separation to be described.

Since the frequency bands of the four source signals are known, it is possible to set reasonable filters according to the frequency bands and extract the signals transmitted from the corresponding loudspeakers. To reduce the requirement for hardware storage, the direct type II structure of the infinite impulse response (IIR) filter [34] is adopted. The difference equation of the P^{th}-order filter is

$$\omega(k) = x(k) - \sum_{p=1}^{P} b_p \omega(k-p) \tag{14}$$

$$y(k) = \sum_{q=0}^{Q} c_q \omega(k-q) \tag{15}$$

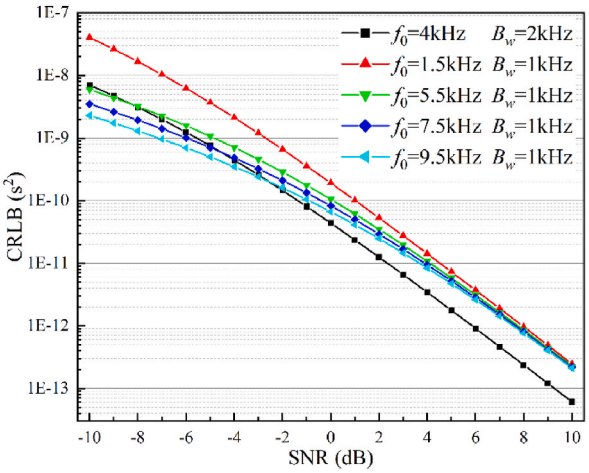

Fig. 5. Cramer-Rao lower bounds for signals with different starting frequencies and bandwidths.

where $x(k)$ and $y(k)$ are the input and out sequence, respectively, and $\omega(k)$ denotes the intermediate variable of type II structure; P and Q are the filters' orders ($P > Q$), and b_p and c_q are filter coefficients.

Since the bandwidths of all source signals' are 1 kHz, an 11th-order Butterworth bandpass filter is used to keep the narrow passband response as flat as possible. All four filters have the same characteristics, but different starting and cutoff frequencies modified based on each characteristic of the individual sound source. The transition bands at both ends of the bandpass filter are set to 350 Hz, taking into account the slope characteristics of the transition bands.

Fig. 6 displays the power spectral density (PSD) of the signals transmitted by Spk0 through Spk3 along with that received by Mic1. The frequency bands of Spk0 through Spk3 are 1.5kHz–2.5 kHz, 5.5kHz–6.5 kHz, 7.5kHz–8.5 kHz, and 9.5 kHz–10.5 kHz, respectively. Mic1 covers a frequency band encompassing all four bands of the loudspeakers, and the PSDs of the effective bands are all greater than −60 dB/Hz with high SNR. Noise less than −70 dB/Hz occurs in the range of the non-effective frequency band, which is almost identical to the characteristics in the acoustic spectrum of Fig. 4(b). As can be seen in Fig. 6 (b), the four signal bands can be extracted after filtering, and the noises in the transition bandwidth can all be eliminated through filtering. The useful frequency bands are, as well mostly identical to that contained in Mic1signal with no excessive interference introduced. In the same manner, the rest of the microphones, and the corresponding acoustic signals are accurately extracted, thus achieving the TOF information being collected simultaneously.

Fig. 6 (c) displays the signal of Mic1 along with the four filtered signals. Despite some attenuation of the signal through the filtration, the TOF calculated is hardly affected due to the fact that neither the degree of correlation nor the peak location of the cross-correlation curve is independent of signal amplitudes to large extent. Hence, the FDM method provides a way that enables the acoustic signals from four loudspeakers to be acquired by one microphone simultaneously and the composite signal to be extracted accurately.

For further verification of the method's accuracy and robustness, numerical simulations and experiments under different test conditions and noise environments were carried out, presented in sections 3 and 4.

The measurement accuracy of the AT system, to a large extent, depends on the accuracy of the calculated TOF. The generalized cross-correlation (GCC) method [49,50] provides one of the primary solutions to the TOF estimation. The cross-power spectrum is obtained by performing a Fourier transform on the two time-domain acoustic signals, and then the inverse Fourier transform is performed to obtain the cross-correlation function [42,51]. The process is as follows:

$$G_{x_1x_2}(\omega) = F[x_1(t)]F^*[x_2(t)] \tag{16}$$

$$R_{x_1x_2}(\tau) = F^{-1}[G_{x_1x_2}(\omega)] \tag{17}$$

where $G_{x1x2}(\omega)$ is the cross-power spectrum of the two signals; $F[\cdot]$ stands for Fourier transform; * denotes the complex conjugate; $R_{x1x2}(\omega)$ is the cross-correlation function; $F^{-1}[\cdot]$ represents the inverse Fourier transform function.

The acoustic TOF is determined by detecting the peak position of the cross-correlation function,

$$\tau = \underset{\tau}{\operatorname{argmax}}[R_{x_1x_2}(\tau)] \tag{18}$$

3. Numerical results and discussion

In this section, the performance of the proposed method, with regard to its feasibility and accuracy is evaluated numerically under different settings of temperature distribution, and the reconstruction quality (RQ) was compared with that of the conventional method using the SART inversion algorithm in MATLAB.

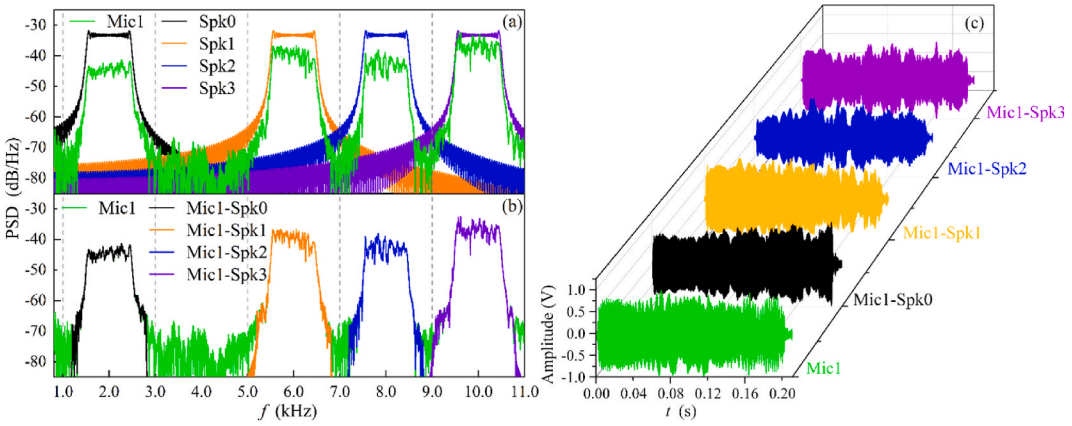

Fig. 6. Power spectral density (PSD) and waveforms of the acoustic signals. (a) PSD of the signals prior to filtering. (b) PSD of the filtered signals. (c) Four acoustic signal waveforms filtered by Mic1 signal.

3.1. Simulation setup

For the simulation, the source signal of the conventional method was a 4–6 kHz Chirp signal, and the four sources of the FDM method were in the frequency bands of 1.5 kHz–2.5 kHz, 5.5 kHz–6.5 kHz, 7.5 kHz–8.5 kHz, and 9.5 kHz–10.5 kHz, respectively, all with the amplitude of 1 V. The array of sensors was arranged as illustrated in Fig. 2, consisting of four loudspeakers and twelve microphones forming 32 transducer pairs to measure the TOFs. For achieving a similar setting as in the experiment, the RoI in the simulation was discretized into 36 pixels in a resolution of 1 m × 1 m assuming a uniform temperature distribution within each pixel. Three typical models of temperature distribution were employed in the verification of the proposed method RQ: the single-peak symmetric, the single-peak asymmetric, and the double-peak asymmetric models. The single-peak and double-peak temperature distribution models can be specified as

$$T(x,y) = 175 \times \exp\left[-\frac{(x-x_1)^2 + (y-y_1)^2}{0.04}\right] + 25 \tag{19}$$

$$T(x,y) = 175 \times \exp\left[-\frac{(x-x_1)^2 + (y-y_1)^2}{0.04}\right] + 135 \times \exp\left[-\frac{(x-x_2)^2 + (y-y_2)^2}{0.04}\right] + 25 \tag{20}$$

where both x_1 and y_1 were 0.5 for the single-peaked symmetric model and 0.4 and 0.6 for the single-peaked asymmetric model; x_1 and y_1 were 0.3 and 0.4, and x_2 and y_2 were 0.5 and 0.3, respectively, for the double-peaked asymmetric model.

The RQ is assessed by the average value of relative error (ARE) [19] and the average root-mean-square error (ARMSE) [19,40], which are defined as follows:

$$\mathrm{ARE} = \frac{1}{n}\sum_{r=1}^{n}\left(\frac{1}{N}\sum_{i=1}^{N}\left|\frac{\widehat{T}_i - T_i}{T_i}\right|\right) \times 100\% \tag{21}$$

$$\mathrm{ARMSE} = \frac{1}{n}\sum_{r=1}^{n}\left(\frac{1}{\overline{T}}\sqrt{\frac{1}{N}\sum_{i=1}^{N}(\widehat{T}_i - T_i)^2}\right) \times 100\% \tag{22}$$

where n is the number of simulations for each set, N is the number of pixels to be solved for, T_i and are the pixel temperature value of that model and the reconstructed one by the AT system, respectively, is the mean value of the temperature model.

3.2. Reconstruction results without noise interference

Firstly, the theoretical signals and TOFs were pre-determined based on the structure size and temperature distribution, and the time delay was added to the acoustic signals corresponding to the 32 channels, then through superposition forming the composite signal received by each microphone.

Secondly, the temperature distribution was inverted based on the inverse problem theory. Conventional and FDM methods were performed in obtaining the TOF estimation and temperature reconstruction. The signal sampling rate in the AT simulation system was set to 1 MS/s, the relaxation factor of the SART algorithm was 1, the maximum number of iterations k was 5000, and the number of

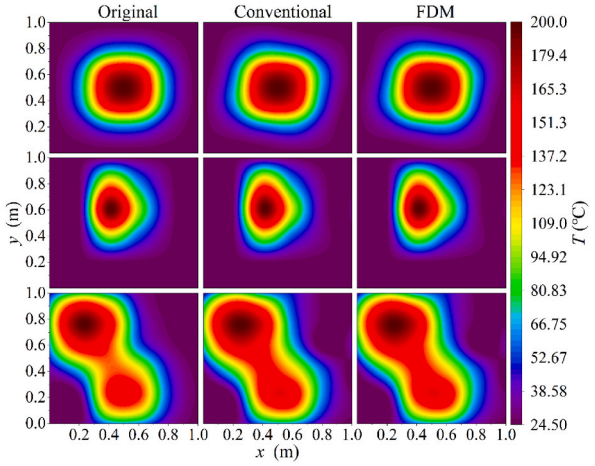

Fig. 7. Reconstruction results of three temperature distribution models by conventional and FDM methods.

inversions n was 2000. The 2-D temperature distribution image of 6 × 6 pixels was reconstructed according to Eq. (6), and then the spatial resolution [52–54] of the AT simulation system was enhanced by the bicubic interpolation method [55–58].

The original temperature distributions of the three models are displayed in the first column of Fig. 7. The second and third columns of Fig. 7 and Table 1 show the reconstructed images and errors of the conventional and FDM methods for the three models. It can be seen that the reconstructed images of the two methods are the same, each having slight differences from the original outer temperature distribution for all three models, which is due to the SART algorithm but not the accuracy of the FDM method. The reconstructed distributions of the single-peaked asymmetric and double-peaked asymmetric models are almost identical to the original. Table I results shows that the RQ of the FDM method is consistent with that of the conventional method in the absence of noise interference, which indicates that the acoustic signal under multiple paths separated from the composite signal by the FDM method is the same as that of the conventional method, hence demonstrating the effectiveness and accuracy of the filtering. This suggests the possibility of replacement of the traditional method with the proposed FDM method for allowing higher temporal reconstruction but without sacrificing spatial resolution. But the FDM method performance in strong noise interference needs to be verified.

3.3. Reconstruction results with noisy interference signals

For investigation of the noise levels effect on the reconstruction of the FDM method, white Gaussian noise (AWGN) with a Mean of 0 and Variance of 1 was introduced and superimposed into the received signals so that the SNR of the received signal by the microphone was varied between 10 dB and −10 dB. The number of simulations, sampling rate, and iterations for each SNR condition was the same as those in Section 3.2.

Fig. 8 shows the reconstruction errors of the conventional and FDM methods for the three temperature distributions with different SNRs. The left and right axes of Fig. 8 (a), (b), and (c) represent ARE and ARMSE, respectively. From comparisons of ARE and ARMSE, the RQs of both methods for the three temperature distributions are almost identical when the SNR is greater than −3 dB, but both tend to deteriorate as the SNR decreases (signified by increased levels of ARE and ARMSE). Although the FDM method's errors are slightly larger than the conventional method, the differences are all relatively quite small. Even in the two-peaked asymmetric model with the maximum reconstruction error, the ARE and ARMSE of the FDM method are only 1.73×10^{-3}% and 1.19×10^{-2}% greater than those of the conventional method. This statistical analysis shows that the reconstruction errors can be regarded as no real difference at different SNRs between the conventional and the FDM methods, implying a similar RQ.

3.4. Reconstruction results of dynamic temperature field

The reconstruction results of the first two sections with and without noise interference show that the difference between the two methods is not obvious under the condition of a constant temperature field. In fact, even at different SNRs, the reconstruction error of the conventional method may be lower. However, as analyzed in Section 2.4, the major advantage of the FDM method is its ability to complete the sampling of acoustic signals on all sound paths simultaneously, which can ensure consistent timing for signal sampling on every path and thus capture the dynamic changes in temperature distribution with high temporal resolution. To evaluate the reconstruction performance of the two methods under the changing temperature field, dynamic temperature field simulation results are presented in this section. In order to have an accurate measurement standard for the reconstruction results of the two methods, the maximum value of the dynamic temperature field model was regulated in the simulation following the sine curve pattern as shown in Fig. 9(a).

According to the timing diagram of the conventional and FDM methods shown in Fig. 3, it can be seen that the time taken for signal generation and acquisition for the FDM method is just a quarter of that for the conventional method. Therefore, in the simulation, in order to ensure that the program setting time does not exceed the maximum actual TOF of each acoustic path, the maximum margin of the TOF τ is set as 0.1 s, and the pulse width τ_s of the source signal is 0.2 s, and the interval time $\Delta\tau$ is 0.1 s. The maximum sampling time for all acoustic signals of the FDM method, therefore, is 0.4 s, while the conventional method is 4 times of it, i.e. 1.6 s. The temperature field dynamic change is assumed to follow a sinusoidal pattern, and the period is 10 s, with a starting bias of 200 °C. The time resolution used is 0.01 s. Under the above settings, a random time is selected to start synchronous measurements using the both methods.

Fig. 9 (b) shows the temperature distribution at the start of the measurement, and in order to quantitatively analyze the reconstruction performance of the two methods, the temperature distribution at the start of the measurement is used as a benchmark for error analysis. Fig. 9 (c) displays the reconstruction result with the conventional method, which exhibits obvious distortion and significant deviation. As indicated in Fig. 2, the emission times of the four speakers with the conventional method are different, and due to the dynamic temperature change, the temperature environment at the time of emission for each loudspeaker is also different, which results in significant variations in the TOF of the corresponding transducer signals. This is the main reason why the conventional reconstruction method cannot capture the dynamic changes in the temperature distribution. Based on statistical analysis, the relative error of the reconstruction with the conventional method is 55.28%, rendering it useless as a reference for diagnosis or control.

Table 1
Reconstruction errors of Conventional and FDM methods for the three temperature distributions.

Temperature distribution Model	Conventional		FDM	
	ARE	ARMSE	ARE	ARMSE
Single-peak Symmetry	3.199	3.422	3.199	3.422
Single-peak Asymmetric	3.264	3.573	3.264	3.573
Double-peak Asymmetric	5.486	6.315	5.486	6.315

Table 2
Reconstruction errors of Conventional and FDM methods for the three cases.

		Conventional	FDM
Case1	ARE	4.42	4.49
	ARMSE	4.94	4.70
Case2	ARE	3.62	3.41
	ARMSE	4.37	3.77
Case3	ARE	4.93	4.11
	ARMSE	4.89	4.52

Case1, Case2, and Case3 in Table II represent the test conditions for the electric furnace positioned on the RoI's left, middle, and right sides, respectively, and the number of measurements was set to 2000 for each case.

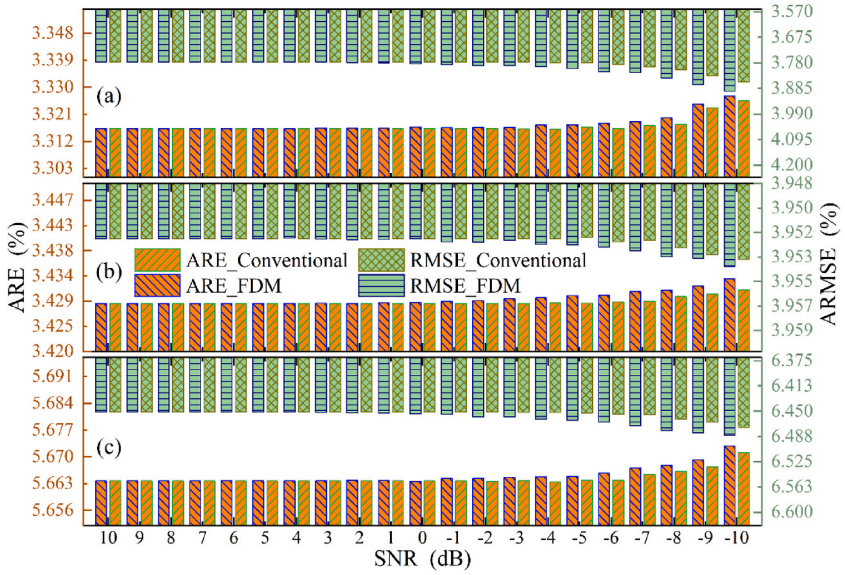

Fig. 8. Reconstruction errors of three temperature distributions with different SNRs for conventional and FDM methods. (a) Single-peak symmetry temperature distribution; (b) Single-peak asymmetric temperature distribution; (c) Double-peak asymmetric temperature distribution.

Fig. 9 (d) shows the reconstruction result with the FDM method, which is very smooth and consistent with the trend of the set-up temperature field model. This is due to the consistency of signal sampling time across multiple acoustic paths, which guarantees the same temperature environment for all acoustic signals. Statistically, the relative reconstruction error with the FDM method is 3.65% when compared with the start moment in Fig. 9 (a). This confirms that the proposed FDM method has better reconstruction accuracy and, moreover, it enables to capture the dynamic changes of the temperature distribution.

4. Experimental results and discussion

In this section, an experimental study is performed to evaluate the reliability and validity of the proposed method. The experimental platform of the AT system developed to reconstruct the temperature distribution is shown in Fig. 10. The RoI was a 1 m × 1 m square, with the exact dimensions, the number of pixels, and sensor mounting positions as shown in Fig. 2. The loudspeakers and microphones were spaced at 0.25 m on each side of the RoI. Four 50W/8Ω, 44-wire core neodymium loudspeakers were driven by a power amplifier to transmit acoustic signals. Twelve omnidirectional microphones (KATELUO KM-2) with a sensitivity of −40dB ± 3 dB and a frequency response of 20 Hz-20kHz were powered by two 8-channel signal conditioners to drive and receive the acoustic signals. The data acquisition equipment was NI PXIe-1073, which consisted of card PXIe-6738 (32 voltage outputs, 16-Bit accuracy, 8-channel simultaneous sampling rate of 1 MS/s, time resolution of 10 ns) and card PXIe-6284 (32 voltage inputs, 16-Bit accuracy, multi-channel maximum sampling rate of 500 kS/s, time resolution of 50 ns). Sixty-four type K thermocouples (GG-K-30-SLE made in Shanghai Yaogeng Automation Instrument Co., Shanghai, China) with a diameter of 0.255 mm were fixed on a square steel mesh frame then acquired by a multi-channel temperature recorder (precision of 0.2% ± 0.5 °C). The AT system also included an electric furnace with a power of 2 kW and a diameter of 40 cm and a computer (CPU Intel(R) Core (TM) i7-10700F CPU @ 2.90 GHz, 16.0 GB).

The electric furnace was placed as a heat source in the RoI area, with the microphone horizontally aligned with the loudspeaker outlet. The distance from the measured level to the furnace was 5 cm. Acoustic foam with a thickness of 5 cm was placed around the electric furnace to reduce the sound's reflection influence. The furnace was covered with a breathable alkali-free glass fiber cloth of 0.3 mm diameter to eliminate interference with the thermocouple from the heat radiation of the electric furnace wire and to ensure the passage of heat. The thermocouple matrix was arranged non-uniformly, i.e., densely packed in the middle and sparsely packed around,

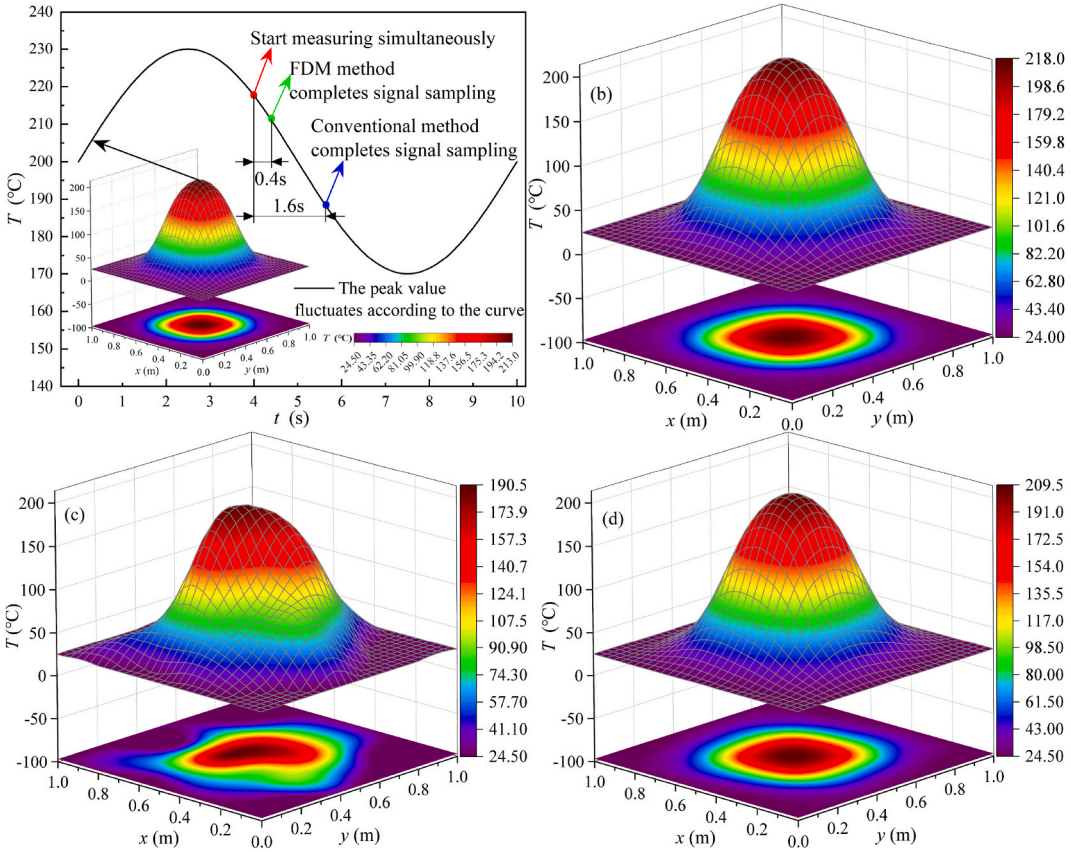

Fig. 9. Simulation results of dynamic temperature field. (a) Temporal variation of peak value in temperature distribution. (b) Temperature field model at the start of measurement; (c) Reconstructed temperature distribution of the conventional method; (d) Reconstructed temperature distribution of the FDM method.

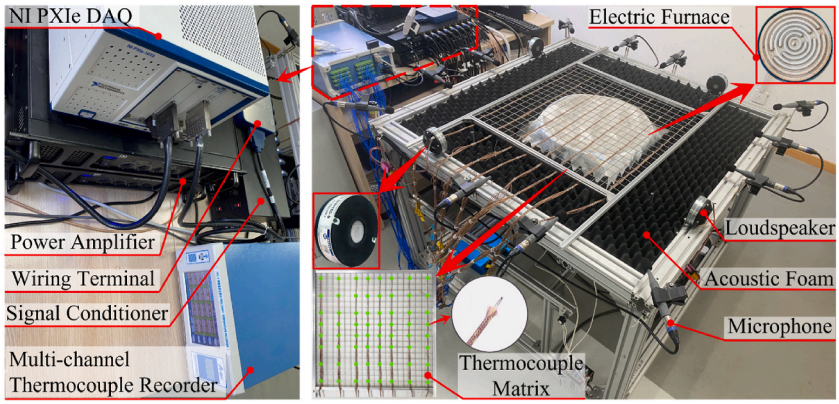

Fig. 10. The experimental platform of the AT system.

with the structure shown in Fig. 10, and the distance of thermocouples from the furnace was 3 cm.

4.1. System error calibration

As shown in Fig. 10, the distance between the loudspeaker outlet and the coil-wrapped sound diaphragm results in a systematic error in the acoustic TOF estimation. Since the system and the sensor structure remain unchanged, this systematic error can be calibrated with the least squares method,

$$\tau_r = \varsigma\tau_e + \Delta\tau_e \tag{23}$$

where τ_r is the actual TOF between the loudspeaker and the microphone derived by dividing the distance measured with a laser distance meter by the average speed of sound (ambient temperature known). τ_e is the TOF estimated by the acoustic GCC method, $\Delta\tau_e$ is the systematic error, and ς is a correction factor due to the waveform distortion error when the acoustic wave varies with the propagation distance. In this experimental system, the correction factor and systematic errors were 1.002283 and 0.140164 ms, respectively, to the extent that the correct TOF could be estimated.

4.2. Temporal resolution analysis

The sound sources in the experiments were set the same as in the numerical simulation, with signal amplitudes of 1 V. The microphone receives the sound after passing through the RoI, processed by the signal conditioner, and passed to the computer via DAQ acquisition. As can be seen from Section 2.5, the conventional method requires four loudspeakers to take turns to transmit acoustic waves and are separately captured by the corresponding microphones to complete a measurement cycle. In contrast, the FDM method allows four loudspeakers to simultaneously transmit acoustic signals of different frequencies while all being received by twelve microphones. Therefore, the theoretical signal acquisition time of the FDM method is 0.25 times that of the conventional. The temporal resolution of the two methods was quantified by performing 2000 consecutive measurements on the experimental platform shown in Fig. 10 and accurately recording the processing time for acoustic signal acquisition, TOF estimation, and temperature reconstruction utilizing LabVIEW software. Both methods adopted the SART algorithm to reconstruct the temperature distribution with an iteration number of 5000 and a relaxation factor of 1. The signal sampling rate was 50 kS/s, and the length of the sampled data was 12.5 k. The interpolation method involved in the experiment was the same as in the simulation. It takes a specific time for the furnace to reach a stable state. After continuous monitoring of the thermocouple, it was found that the time from start-up to the stability of the furnace was about 35 min, and the experiment was set up after 40 min of furnace start-up.

The time recorded by the system is shown in Fig. 11. The signal sampling time of the FDM method is much shorter than that of the conventional. The average time of signal sampling for the two methods were statistically 502.088 ms and 2000.941 ms, and that of TOF estimation and temperature inversion were 1083.926 ms and 1089.693 ms, respectively. One can see that the TOF estimation (signal processing) and inversion time of the two methods are almost identical, with a significant difference only in the signal acquisition stage. The time fluctuations of the signal sampling for both methods are about $\pm$5.6 ms, and of the calculation, about $\pm$10.4 ms, which are caused by the variation of the computer load and are insignificant compared to the sampling and calculation times. The comparison results show that the signal acquisition time of the proposed FDM method is 0.251 times longer than that of the conventional method, which dramatically improves the temporal resolution of the temperature field reconstruction.

4.3. Analysis of measurement results

To verify the accuracy of the FDM method, the electric furnace mounted on a sliding track using a bracket, was moved to the left, middle, and right of the RoI, and the matrix of thermocouples was moved accordingly measuring the signals with the acoustic method after the 40 min furnace start-up period. The thermocouple matrix was mainly arranged directly above the furnace, along with several individual thermocouples measuring the temperature at the remaining locations of the RoI applied to the overall reconstruction as an a priori condition of the ambient temperature.

Fig. 12 shows the reconstructed temperature distributions of the same time, obtained by the thermocouple matrix, conventional, and FDM methods, for the locations of right, middle, and left. It is seen that both acoustic methods can accurately reconstruct the correct locations and temperature distributions of the furnace and achieved similar results to the thermocouple detected ones. Since the furnace surface was slightly below the measurement plane and the gas flow was limited by the acoustic foam, the ambient temperature fluctuations within the RoI were minor, which led to an apparent difference between the thermocouple readings and the ambient temperature, the thermocouple resulted in significant square edges even after interpolation. The overall temperature reconstruction results were slightly lower than those of the thermocouples, implied by the slightly smaller constructed areas from the acoustic methods. This can be explained as due to the fact that the measurement plane of the acoustic method was further away from the furnace surface compared to the locations of the thermocouple matrix. But, comparing the two acoustic methods, since the FDM method has a shorter measurement period and better real-time performance, its reconstruction results showed more close agreement with the thermocouples'. The respective relative errors of the maximum temperatures of the conventional and FDM methods versus the thermocouples' were 4.1% and 2.8%.

Since the reconstructed temperature results in the non-high temperature region of the RoI were interpolated with the results of several representative thermocouples only, the assessment results given in the table were derived for the region of 0.4 m $\times$ 0.4 m where the matrix of thermocouples positioned so as to achieve a more accurate quantitative comparison of the RQ. The FDM and Conventional methods perform best in Case 2 as they both have minimal errors. Case1 and Case3 have similar RQ, but both methods have relatively poorer inversion results. In the three cases, the reconstruction errors of both methods were less than 5%, and the ARE and ARMSE of the FDM method were 0.32% and 0.40% lower than those of the conventional method, respectively, indicating that the proposed FDM method can achieve the same or even better reconstruction results than the conventional method.

5. Conclusion

This paper proposes an AT system based on the FDM method, which can significantly improve the temporal resolution of temperature distribution reconstruction.

Through theoretical analysis, numerical simulation, and experiment test, the feasibility of the acoustic FDM method was verified, and the reason for its time reduction was explained which is based on the principle of concurrent multi-channel transmissions, instead

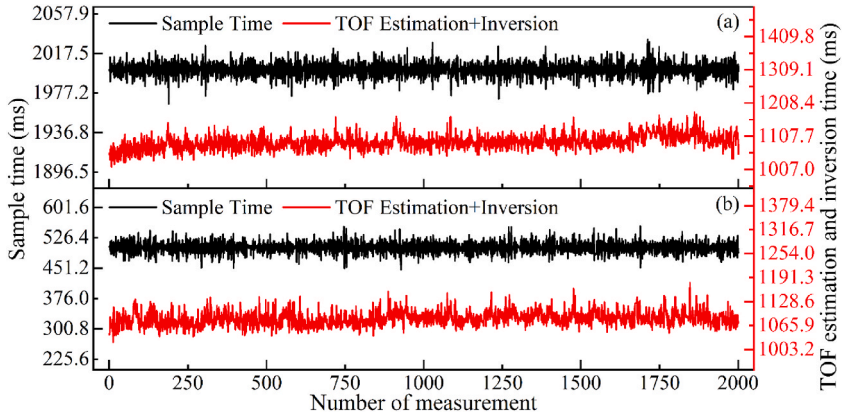

Fig. 11. Processing time of signal acquisition, TOF estimation, and inversion for conventional and FDM methods. (a) Recording time of conventional method; (b) Recording time of FDM method.

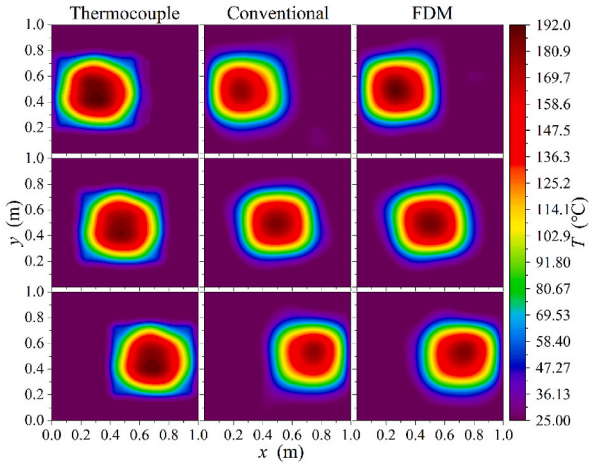

Fig. 12. The reconstructed temperature distribution for thermocouple, conventional, and FDM methods.

of the conventional manner of sequential transmission, avoided time wastage in channel switchings. Thus the FDM method reduces the time of acoustic signal acquisition to a quarter (0.251) times of the conventional method's, leading to a significant improvement in the system's temporal resolution (3.98 times improvement). For evaluation of the FMD method performance, reconstructions of the high-temperature regions were conducted using three methods: thermocouple, acoustic conventional, and FDM methods, and the accuracy of the FDM method was evaluated by location variation of the high-temperature region. Due to fact of the higher temporal resolution of the FDM method, the dynamic temperature variations could be captured more accurately, and the respective ARE and ARMSE of which were 0.32% and 0.40% lower than those of the conventional method. It can be concluded that with the FDM method, a more accurate temperature distribution reconstruction can be achieved while ensuring a high temporal resolution.

Despite the verification of the accuracy and robustness of the AT system through experiments under several test conditions, there might be some limitations for the proposed FDM method in field applications. Firstly, if there are severe gas medium turbulence or backflow occurs within the RoI, it may lead to additional errors in the method's results. Secondly, the acoustic signals concerned in this paper were all in the audible acoustic band, which was limited by the difference in sensors, therefore the proposed method is not suitable for applications of ultrasonic tomography for the time being. Thirdly, when the number of loudspeakers is increased to provide more acoustic paths, although there is no limitation on the number of sensors to be used in the FDM method, the number of signals set by distinctions of the frequency band cannot be increased without restriction owing to the limitation of the frequency response of both the loudspeakers and microphones.

Author statement

Qi Liu: Ideas, Methodology, Software. **Bin Zhou**: Formal analysis, Resources, Supervision. **Ruixue Cheng**: Visualization, Investigation. **Jianyong Zhang**: Data Curation, Software. **Rong Zhao**: Discussion and guidance on experimental details. **Minglu Dai**: Data Curation, Software. **Xuhao Zhao**: Assist with experiments. **Yihong Wang**: Writing- Reviewing and Editing.

Declaration of competing interest

The authors declare that they have no known competing financial interests or personal relationships that could have appeared to influence the work reported in this paper.

Data availability

Data will be made available on request.

Acknowledgments

This work was supported in part by the National Natural Science Foundation of China under Grant NO. 50976024 and NO. 50906013, the National Key Research and Development Program of China under Grant NO. 2017YFB0603204. The authors would like to thank the anonymous reviewers for their time and valuable comments.

References

[1] M. Bramanti, E.A. Salerno, A. Tonazzini, S. Pasini, A. Gray, An acoustic pyrometer system for tomographic thermal imaging in power plant boilers, IEEE Trans. Instrum. Meas. 45 (1996) 159–167, https://doi.org/10.1109/19.481329.
[2] U. Sarma, P.K. Boruah, Design and development of a high precision thermocouple based smart industrial thermometer with on line linearisation and data logging feature, Measurement 43 (2010) 1589–1594, https://doi.org/10.1016/j.measurement.2010.09.003.
[3] M. Schalles, F. Bernhard, Triple-fixed-Point blackbody for the calibration of radiation thermometers, Int. J. Thermophys. 28 (2007) 2049–2058, https://doi.org/10.1007/s10765-007-0277-9.
[4] D. Bradley, K.J. Matthews, Measurement of high gas temperatures with fine wire thermocouples, J. Mech. Eng. Sci. 10 (1968) 299–305, https://doi.org/10.1243/jmes_jour_1968_010_048_02.
[5] C. Liu, L.J. Xu, Laser absorption spectroscopy for combustion diagnosis in reactive flows: a review, Appl. Spectrosc. Rev. 54 (2019) 1–44, https://doi.org/10.1080/05704928.2018.1448854.
[6] Y. Wang, B. Zhou, C. Liu, Calibration-free wavelength modulation spectroscopy based on even-order harmonics, Opt Express 29 (2021) 26618–26633, https://doi.org/10.1364/OE.432361.
[7] Y. Wang, B. Zhou, R. Zhao, B. Wang, Q. Liu, M. Dai, Super-accuracy calculation for the half width of a voigt profile, Mathematics 10 (2022) 210, https://doi.org/10.3390/math10020210.
[8] W. Wei, J.W. Yu, T. You, X.F. Yu, Y.H. Wang, Evaluation of the transient temperature distribution of end-face sliding friction pair using infrared thermometry, Key Eng. Mater. 613 (2014) 213–218. http://www.ogp-cn.com/EN/10.4028/www.scientific.net/kem.613.213.
[9] V.E. Mosharov, V.N. Radchenko, I.V. Senyuev, Pyrometry using CCD cameras, Instrum. Exp. Tech. 56 (2013) 491–496, https://doi.org/10.1134/s0020441213030214.
[10] M. Dai, B. Zhou, J. Zhang, B. Zuo, Y. Wang, Experimental and simulation investigation of 3-D soot temperature and volume fraction fields of afterburner flame, Case Stud. Therm. Eng. 33 (2022), 101932, https://doi.org/10.1016/j.csite.2022.101932.
[11] Q. Kong, G. Jiang, Y. Liu, M. Yu, Numerical and experimental study on temperature field reconstruction based on acoustic tomography, Appl. Therm. Eng. 170 (2020), 114720, https://doi.org/10.1016/j.applthermaleng.2019.114720.
[12] Y. Bao, J. Jia, Online time-resolved reconstruction method for acoustic tomography system, IEEE Trans. Instrum. Meas. 69 (2020) 4033–4041, https://doi.org/10.1109/tim.2019.2947949.
[13] M. Barth, A. Raabe, Acoustic tomographic imaging of temperature and flow fields in air, Meas. Sci. Technol. 22 (2011), 035102, https://doi.org/10.1088/0957-0233/22/3/035102.
[14] S. Zhang, G. Shen, L. An, Y. Niu, Online monitoring of the two-dimensional temperature field in a boiler furnace based on acoustic computed tomography, Appl. Therm. Eng. 75 (2015) 958–966, https://doi.org/10.1016/j.applthermaleng.2014.10.085.
[15] Ł. Śladewski, K. Wojdan, K. Świrski, T. Janda, D. Nabagło, J. Chachuła, Optimization of combustion process in coal-fired power plant with utilization of acoustic system for in-furnace temperature measurement, Appl. Therm. Eng. 123 (2017) 711–720, https://doi.org/10.1016/j.applthermaleng.2017.05.078.
[16] L. Zhang, J. Li, Acoustic tomography temperature reconstruction based on virtual observation and residual network, IEEE Sensor. J. (2022) 1, https://doi.org/10.1109/JSEN.2022.3192924, 1.
[17] S. Liu, S. Liu, G. Tong, Reconstruction method for inversion problems in an acoustic tomography based temperature distribution measurement, Meas. Sci. Technol. 28 (2017), 115005, https://doi.org/10.1088/1361-6501/aa8589.
[18] U. DeSilva, R.H. Bunce, H. Claussen, Novel Gas Turbine Exhaust Temperature Measurement System, American Society of Mechanical Engineers Digital Collection, 2013, https://doi.org/10.1115/gt2013-95152.
[19] S. Liu, S. Liu, T. Ren, Acoustic tomography reconstruction method for the temperature distribution measurement, IEEE Trans. Instrum. Meas. 66 (2017) 1936–1945, https://doi.org/10.1109/tim.2017.2677638.
[20] Z. Hu, S. Tariq, T. Zayed, A comprehensive review of acoustic based leak localization method in pressurized pipelines, Mech. Syst. Signal Process. 161 (2021), 107994, https://doi.org/10.1016/j.ymssp.2021.107994.
[21] Y. Bao, J. Jia, N. Polydorides, Real-time temperature field measurement based on acoustic tomography, Meas. Sci. Technol. 28 (2017), 074002, https://doi.org/10.1088/1361-6501/aa6e26.
[22] S. Pal, F.-S. Lin, C.-C. Hsieh, M.-C. Huang, C.-Y. Lee, Y.-H. Liu, C.-Y. Lu, S.-W. Du, C.-H. Huang, Acoustic speed measurement platform for monitoring highly concentrated gas temperature distribution, IEEE Sensors Letters 6 (2022) 1–4, https://doi.org/10.1109/LSENS.2022.3153354.
[23] S.P. Zhang, Acoustic pyrometry system for environmental protection in power plant boilers, Journal of Environmental Informatics 23 (2014) 24–35, https://doi.org/10.3808/jei.201400265.
[24] S. Zhang, G. Geng, Z. Li, Y. Zhang, Fast implementation of area integral model SART algorithm based on look-up table, Cluster Comput. 22 (2019) 15195–15203, https://doi.org/10.1007/s10586-018-2533-0.
[25] T. Yu, W. Cai, Benchmark evaluation of inversion algorithms for tomographic absorption spectroscopy, Appl. Opt. 56 (2017) 2183, https://doi.org/10.1364/AO.56.002183.
[26] D. Kazantsev, G.V. Eyndhoven, W.R.B. Lionheart, P.J. Withers, K.J. Dobson, S.A. McDonald, R. Atwood, P.D. Lee, Employing temporal self-similarity across the entire time domain in computed tomography reconstruction, Phil. Trans. Math. Phys. Eng. Sci. 373 (2015), 20140389, https://doi.org/10.1098/rsta.2014.0389.
[27] A.H. Andersen, A.C. Kak, Simultaneous algebraic reconstruction technique (SART): a superior implementation of the ART algorithm, Ultrason. Imag. 6 (1984) 81–94, https://doi.org/10.1016/0161-7346(84)90008-7.
[28] W. Cai, C.F. Kaminski, Tomographic absorption spectroscopy for the study of gas dynamics and reactive flows, Prog. Energy Combust. Sci. 59 (2017) 1–31, https://doi.org/10.1016/j.pecs.2016.11.002.
[29] H. Yan, Y. Wei, Y. Zhou, Y. Wang, Temperature distribution reconstruction method for acoustic tomography based on compressed sensing, Ultrason. Imag. 44 (2022) 77–95, https://doi.org/10.1177/01617346221092695.

[30] J. Lei, W. Liu, S. Liu, Q. Liu, Multiscale reconstruction algorithm for compressed sensing, ISA (Instrum. Soc. Am.) Trans. 53 (2014) 1152–1167, https://doi.org/10.1016/j.isatra.2014.05.001.
[31] J. Provost, F. Lesage, The application of compressed sensing for photo-acoustic tomography, IEEE Trans. Med. Imag. 28 (2009) 585–594, https://doi.org/10.1109/TMI.2008.2007825.
[32] J. Song, Y. Hong, G. Wang, H. Pan, Algebraic tomographic reconstruction of two-dimensional gas temperature based on tunable diode laser absorption spectroscopy, Appl. Phys. B 112 (2013) 529–537, https://doi.org/10.1007/s00340-013-5435-0.
[33] P.C. Hansen, Analysis of discrete ill-posed problems by means of the L-curve, SIAM Rev. 34 (1992) 561–580, https://doi.org/10.1137/1034115.
[34] Q. Liu, B. Zhou, R. Cheng, J. Zhang, Y. Wang, High temporal resolution pyrometry and velocimetry based on acoustic frequency division multiplexing, IEEE Trans. Instrum. Meas. 71 (2022) 1–11, https://doi.org/10.1109/TIM.2022.3141169.
[35] S.F. Green, Acoustic Temperature and Velocity Measurement in Combustion Gases, Begel House Inc., 1986, https://doi.org/10.1615/IHTC8.2670.
[36] I. Jovanovic, A. Hormati, L. Sbaiz, M. Vetterli, Efficient and stable acoustic tomography using sparse reconstruction methods, in: 19th International Congress on Acoustics, 2021. Madrid.
[37] Z. Dogan, I. Jovanovic, T. Blu, D.V.D. Ville, 3D reconstruction of wave-propagated point sources from boundary measurements using joint sparsity and finite rate of innovation, in: 2012 9th IEEE International Symposium on Biomedical Imaging, ISBI), 2012, pp. 1575–1578, https://doi.org/10.1109/ISBI.2012.6235875.
[38] H. Zhou, J. Yan, Numerical and experimental investigations on the total-variation regularization method of temperature distribution reconstruction in acoustic tomography, Meas. Sci. Technol. 32 (2020), 035112, https://doi.org/10.1088/1361-6501/abc204.
[39] G.T. Herman, A. Lent, P.H. Lutz, Relaxation methods for image reconstruction, Commun. ACM 21 (1978) 152–158, https://doi.org/10.1145/359340.359351.
[40] Y. Yu, Q. Xiong, Q. Li, C. Wu, M. Gao, K. Wang, A hybrid kernel function approach for acoustic reconstruction of temperature distribution, Measurement 166 (2020), 108238, https://doi.org/10.1016/j.measurement.2020.108238.
[41] J. Liu, L. Liang, W. Min, Transit Time Measurement for Ultrasonic Tomographic Velocimeters, 2017.
[42] Q. Liu, B. Zhou, J. Zhang, R. Cheng, X. Zhao, R. Zhao, M. Dai, B. Wang, Y. Wang, A time-of-flight estimation method for acoustic ranging and thermometry based on digital lock-in filtering, Sensors 22 (2022) 5519, https://doi.org/10.3390/s22155519.
[43] S. Zhang, G. Shen, L. An, Online monitoring of furnace exit gas temperature in power plants, Appl. Therm. Eng. 147 (2019) 917–926, https://doi.org/10.1016/j.applthermaleng.2018.11.004.
[44] T. Ma, Y. Liu, C. Cao, Neural networks for 3D temperature field reconstruction via acoustic signals, Mech. Syst. Signal Process. 126 (2019) 392–406, https://doi.org/10.1016/j.ymssp.2019.02.037.
[45] R.P. Hebbar, P.G. Poddar, Generalized frequency division multiplexing–based acoustic communication for underwater systems, Int. J. Commun. Syst. 33 (2020), e4292, https://doi.org/10.1002/dac.4292.
[46] A. Kaizer, Modeling of the nonlinear response of an electrodynamic loudspeaker by a volterra series expansion, J. Audio Eng. Soc. 35 (2012).
[47] S. Peleg, B. Porat, The Cramer-Rao lower bound for signals with constant amplitude and polynomial phase, IEEE Trans. Signal Process. 39 (1991) 749–752, https://doi.org/10.1109/78.80864.
[48] M.A. Richards, Fundamentals of Radar Signal Processing, third ed., 2022.
[49] D. Sarwate, M. Pursley, Cross-correlation properties of pseudo-random and related sequences, Proc. IEEE 68 (1980) 593–619, https://doi.org/10.1109/PROC.1980.11697.
[50] B. Podobnik, H.E. Stanley, Detrended cross-correlation analysis: a new method for analyzing two nonstationary time series, Phys. Rev. Lett. 100 (2008), 084102, https://doi.org/10.1103/PhysRevLett.100.084102.
[51] Q. Liu, B. Zhou, R. Zhao, M. Dai, B. Wang, Y. Wang, Development of acoustic thermometer and velocimeter with high temporal resolution and noise suppression capability, in: 2022 11th International Conference on Communications, Circuits and Systems, ICCCAS), Singapore, 2022, pp. 71–74, https://doi.org/10.1109/ICCCAS55266.2022.9824463.
[52] R. Zeyde, M. Elad, M. Protter, On single image scale-up using sparse-representations, in: Curves and Surfaces, Springer, Berlin, Heidelberg, 2012, pp. 711–730, https://doi.org/10.1007/978-3-642-27413-8_47.
[53] X. Zhang, A new kind of super-resolution reconstruction algorithm based on the ICM and the bicubic interpolation, in: 2008 International Symposium on Intelligent Information Technology Application Workshops, 2008, pp. 817–820, https://doi.org/10.1109/IITA.Workshops.2008.12.
[54] A. Paul, P. Warbal, A. Mukherjee, S. Paul, R.K. Saha, Exploring polynomial based interpolation schemes for photoacoustic tomographic image reconstruction, Biomed. Phys. Eng. Express. 8 (2021), 015019, https://doi.org/10.1088/2057-1976/ac3fe6.
[55] R. Keys, Cubic convolution interpolation for digital image processing, IEEE Trans. Acoust. Speech Signal Process. 29 (1981) 1153–1160, https://doi.org/10.1109/tassp.1981.1163711.
[56] F. Aràndiga, A nonlinear algorithm for monotone piecewise bicubic interpolation, Appl. Math. Comput. 272 (2016) 100–113, https://doi.org/10.1016/j.amc.2015.08.027.
[57] Y. Zhang, Y. Li, J. Zhen, J. Li, R. Xie, The hardware realization of the bicubic interpolation enlargement algorithm based on FPGA, in: 2010 Third International Symposium on Information Processing, 2010, pp. 277–281, https://doi.org/10.1109/ISIP.2010.82.
[58] S. Lee, G. Wolberg, S.Y. Shin, Scattered data interpolation with multilevel B-splines, IEEE Trans. Visual. Comput. Graph. 3 (1997) 228–244, https://doi.org/10.1109/2945.620490.